Design of a Transparent Metamaterial Cross Polarization Converter With Large Incident Angle Range

Senfeng Lai, Yanghui Wu, and Wenhua Gu

***Abstract*—In recent years, the metamaterial has become a popular and powerful tool in the electromagnetic polarization conversion design. In this paper, a flexible and transparent broadband cross-polarization-converter (CPC) was designed, fabricated and tested. ANSYS HFSS was used for the cross-polarization-converter simulation, and the Floquet port and master-slave boundary condition were set in the software. The multi-layer split-ring-resonator (SRR) structure was used to form the metamaterial for the CPC. As a result, >77% polarization conversion ratio (PCR) was achieved in the range of (7.8-18.2) GHz, with little change within 45° incident angle. The experimental results were consistent with the simulation data.**

***Index Terms*—Reflective polarization converter, flexible, transparent.**

I. Introduction

THE cross-polarization-converter (CPC) is one of the key members in the family of electromagnetic (EM) wave manipulation devices [1]–[4], and has a wide range of applications in areas including anti-interference, analytical chemistry, biology, communication, imaging, and so on. Although natural anisotropic materials can be used to manipulate EM wave polarization, it is difficult to achieve polarization conversion in the microwave frequency due to the small difference of EM parameters in two orthogonal directions [5]. The metamaterial polarization converters can easily tweak the EM parameters in two orthogonal directions in a large amount, especially effective in the microwave band. However, most of the metamaterial-based CPCs have the drawback of narrow bandwidth [6]–[7]. To extend the bandwidth, stacking multiple layers of complementary structures are generally required [8]–[10]. Another concern is how to maintain excellent polarization conversion ratio (PCR) with large incident angle range [11]. Other limitations of traditional polarization converters include lacking mechanical flexibility and optical transparency, which are required in many novel application scenes. Researches aiming at solving the above limitations of CPC are emerging in recent years [1]–[2].

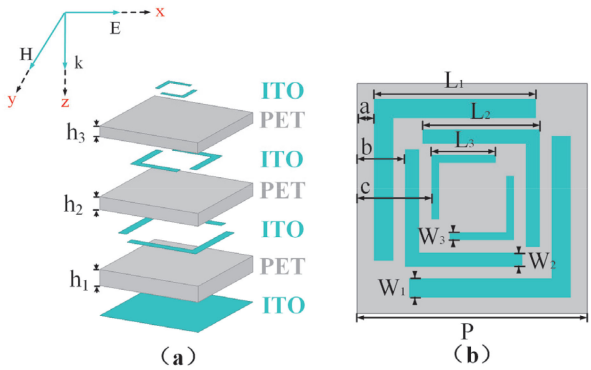

Fig. 1. (a) The 3-D schematic diagram and (b) top view of the structure of the designed CPC.

Nowadays, different types of polarization converters based on anisotropic [12], [13] or chiral [14] metasurfaces have been proposed. In addition, different design solutions have been proposed in order to extend the bandwidth. In fact, metasurfaces have been widely used in the design of polarization converters [15]. Recently, more efforts have focused on miniaturized polarization converters with higher conversion efficiency and wider bandwidth or multiband and also more efforts have focused on miniaturized polarization converters with higher conversion efficiency and wider bandwidth or multi-band [16]–[18]. This has become an urgent need for practical applications.

In this paper, a broadband polarization converter with PCR>77% in the range of (7.8-18.2) GHz was designed and fabricated. The experimental results were consistent with the simulation data. The designed device is insensitive to oblique incidence within 45° range. What is more, the CPC has high optical transparency and good mechanical flexibility.

II. Design of the Transparent Metamaterial

ANSYS HFSS 15.0 was used for the cross-polarization-converter spectrum simulation, and the Floquet port, master-slave boundary condition and adaptive meshing were set in the software. [19], [20]. The reflective CPC was designed using a three-layer SRR structure [21], as shown in Fig. 1. The SRR

Manuscript received June 28, 2021; revised August 3, 2021; accepted August 21, 2021. Date of publication August 24, 2021; date of current version September 3, 2021. This work was supported in part by the Young Innovative Talents Project, Guangdong Province (2019KQNCX069), in part by Special Fund for Science and Technology Innovation Strategy of Guangdong Province (Climbing plan, pdjh2020b0344), and in part by Guangzhou Science and Technology Innovation Development Special Fund Project. *(Corresponding author: Yanghui Wu.)*

Senfeng Lai is with the School of Electronic and Information, Guangdong Polytechnical Normal University, Guangzhou 510665, China (e-mail: laisenfeng@gpnu.edu.cn).

Yanghui Wu and Wenhua Gu are with the School of Electronic and Optical Engineering, Nanjing University of Science and Technology, Nanjing 210094, China (e-mail: 316104002471@njust.edu.cn; guwenhua@njust.edu.cn).

Digital Object Identifier 10.1109/JPHOT.2021.3107359

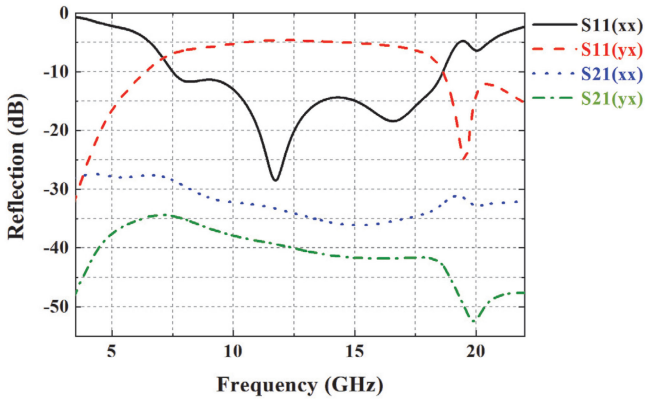

Fig. 2. Reflection and transmission coefficient curves of co-polarization and cross-polarization.

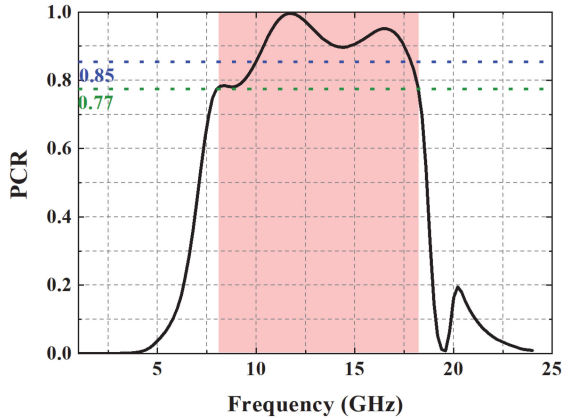

Fig. 3. PCR curve of the designed broadband polarization converter.

structures are of different sizes for each layer, and used indium tin oxide (ITO) as the conductor, polyethylene terephthalate (PET) as the dielectric. An ITO conductive layer was used as the backplane to assure zero EM wave transmission. Both ITO and PET are optically transparent. The period of the optimized unit structure is $p = 10$ mm, the arm width of the bottom SRR is $W_1 = 0.8$ mm, the arm length $L_1 = 7$ mm, $a = 0.5$ mm, the thickness of the bottom dielectric layer is $h_1 = 1.5$ mm; the arm width of the middle SRR is $W_2 = 0.7$ mm, the arm length $L_2 = 4.7$ mm, $b = 2$ mm, the thickness of the middle dielectric layer is $h_2 = 1.2$ mm; the arm width of the top SRR is $W_3 = 0.4$ mm, the arm length $L_3 = 2.4$ mm, $c = 3.2$ mm, the thickness of the top dielectric layer is $h_3 = 1$ mm. The dielectric constant of the PET dielectric layer is $\varepsilon_r = 3$. ITO thin films used in both FSS layers and backplane with a thickness of $h = 185 \pm 5nm$were coated on the PET films by magnetron sputtering. The surface resistance of the ITO material is 8 Ω/sq. The unit structures are periodically repeated to cover the entire sample surface, and the size of the fabricated sample was 310 mm $*$ 290 mm with the total thickness of 3.7 mm.

All simulations in this work were performed by the software High Frequency Structure Simulator (HFSS). The backplane of the multilayer structure is covered by the transparent and conductive material ITO, so that the power transmittance through the structure T can be ignored. The transmittance curves in both x and y directions, S21(xx) and S21(yx), are also shown in Fig. 2. It can be seen from Fig. 2 that the transmittance in both directions are negligible, i.e., less than -28 dB in the whole band, and mostly less than -30 dB. So the equation for calculating the power absorption ratio A can be simplified as:$A = 1 - R - T \approx 1 - |S_{11}|^2 - 0$, where R is the power reflection ratio, and S_{11} is the first element of the S parameter matrix. The co-polarization reflection coefficient can be expressed as:$S_{11}(xx) = r_{xx} = |E_{rx}|/|E_{ix}|$, $S_{11}(yy) = r_{yy} = |E_{ry}|/|E_{iy}|$; while the cross-polarization reflection coefficient can be expressed as:$S_{11}(yx) = r_{yx} = |E_{ry}|/|E_{ix}|$, $S_{11}(xy) = r_{xy} = |E_{rx}|/|E_{iy}|$. Since the designed SRR is axisymmetric along the diagonal of the square period, the simulation results obtained with x-polarized incident field are the same as the results obtained with y- polarized incident field. Therefore, only the case of the x-polarization incident field is discussed and analyzed. The reflection coefficients of co-polarization and cross-polarization are shown as in Fig. 2, showing excellent polarization conversion effects in the range of (7.8–18.2) GHz.

The PCR of the CPC designed in this paper was calculated using $PCR = |R_{yx}|/(|R_{yx}| + |R_{xx}|)$, where cross-polarization reflectivity is $R_{yx} = |S_{11(yx)}|^2$, and co-polarization reflectivity is $R_{xx} = |S_{11(xx)}|^2$. The variable-control method was used to optimize the parameters in the full-wave simulation and to finally determine the optimal parameters. Because of the large number of parameters, the optimization process was not described in detail in the paper. Among them, the parameter that has the greatest influence on the result is the arm length of the resonant ring. The length of the three arm lengths will greatly affect the value and bandwidth of PCR. The PCR spectrum is shown in Fig. 3. It can be seen that PCR$>77\%$ in the (7.8-18.2) GHz range (the red region), and PCR $>85\%$ in the range of (10-17.8) GHz. The curve shows three peak resonant frequency points, which are 8.2 GHz, 11.8 GHz and 16.4 GHz, respectively.

The key to realize polarization conversion is to build up a 180° phase difference between the two orthogonal components of the reflected field. As shown in Fig. 4. (a), the incident field E_i polarized in x-direction can be decomposed into two components: E_{iv}, E_{iu} in the uv coordinates, which is a common practice in similar researches and has been proven to be correct and helpful [22], [23]: E_{iv}, E_{iu} in the uv coordinates. Then E_i can be described as $\vec{E_i} = \hat{u}\, E_{iu} e^{j\phi} + \hat{v}\, E_{iv} e^{j\phi}$. Similarly, the reflection field E_r can also be decomposed into two components in the uv coordinates: E_{rv}, E_{ru}, and then E_r can be described as $\vec{E_r} = \hat{u}\, E_{iu} e^{(j\phi+\phi_u)} + \hat{v}\, E_{iv} e^{(j\phi+\phi_v)}$. When complete cross-polarization occurs, the reflection field E_r must be perpendicular to the x direction, and the E_{rv} and E_{iv} are equal in magnitude but opposite in direction, while the magnitude and direction of E_{ru} and E_{iu} are the same. Then the phase difference $\Delta\varphi$=$|\phi_u - \phi_v|$ between E_{rv} and E_{ru} is about 180°. In Fig. 4. (b), the phase difference between E_{rv} and E_{ru} in the (7.8-18.2) GHz band is shown to be close to 180°, thus achieving wideband polarization conversion.

The co-polarization and cross-polarization reflection coefficients at different incident angles were simulated, as shown

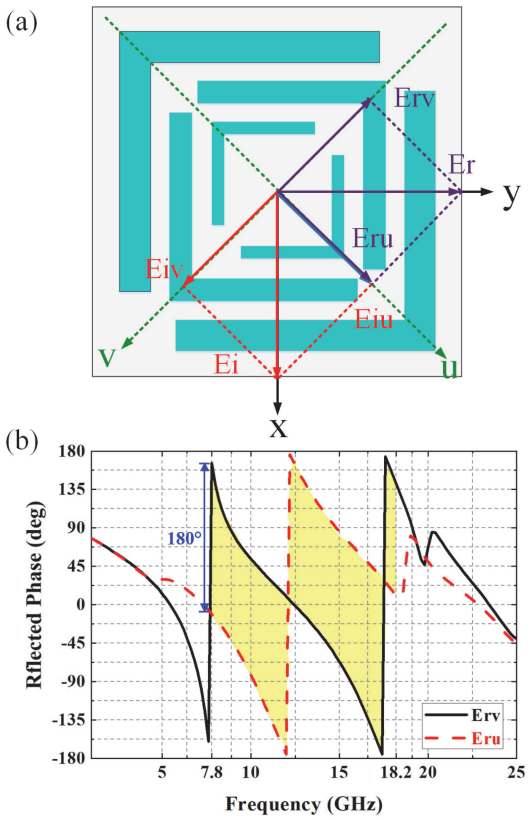

Fig. 4. (a) Illustration of the electric field decomposition for cross-polarization; (b) reflection phase difference between two orthogonal electric field components.

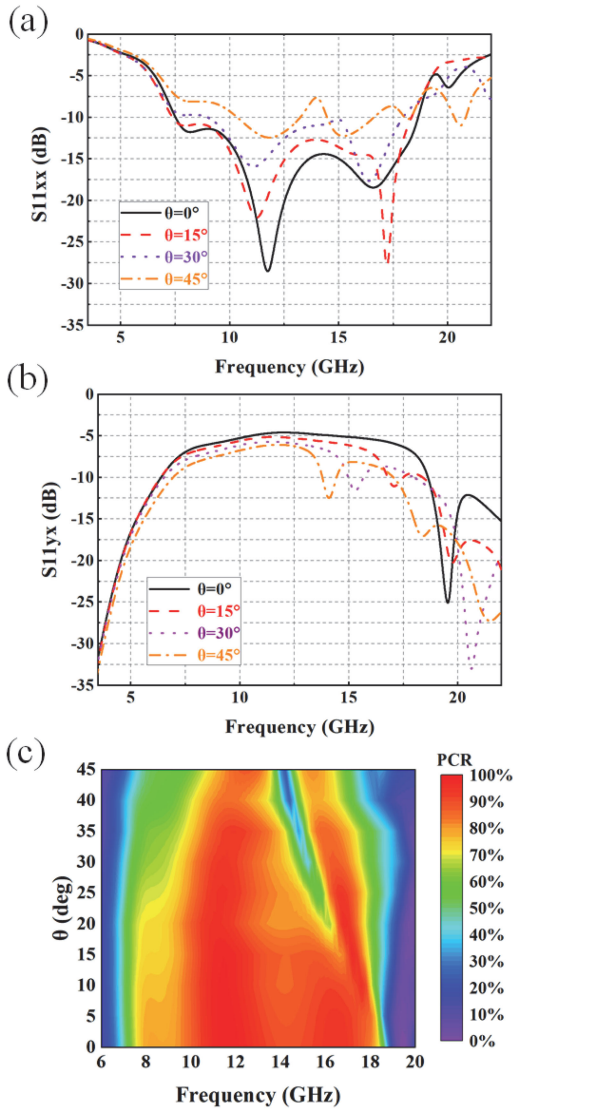

Fig. 5. The reflection coefficient spectrum of (a) co-polarization, (b) cross-polarization at different incident angles, and (c) analytically calculated profile of absorption versus frequency and incident angle for TE polarization.

in Fig. 5. It can be seen that the co-polarization reflection coefficients of the designed CPC change little when the obliquely incident angle is within 30°. For the cross-polarization, the reflection coefficient changes little when the obliquely incident angle is within 45°. Therefore, the CPC designed in this work has the merit of wide incident angle.

III. Fabrication, Testing and Analysis of the Designed CPC

The flexible, transparent and broadband CPC designed above was fabricated and tested, as shown in Fig. 6. (d). The ITO was sputtered onto PET substrate, followed with wet-etching to obtain the proposed structure shown in Fig. 1. The whole fabrication process was very straightforward and used mature industrial techniques, with high potential of mass production. Thanks to the carefully selected materials, the polarization converter is optically transparent and mechanically flexible. These characteristics render the CPC more application freedom.

The Agilent N5232A vector network analyzer was used to measure the co-polarization and cross-polarization reflection coefficients of the metamaterial CPC sample. Two broadband horn antennas covering (1–18) GHz were used, one as the transmitter and the other as the receiver. For the co-polarized reflection (R*xx*) test, both antennas were placed in the horizontal direction (*x*-polarization); while for the cross-polarized reflection (R*yx*) test, the transmitting antenna was in the horizontal direction (*x*-polarization) and the receiving antenna was in the vertical direction (*y* polarization).The comparison between the simulation and measurement results of the co-polarization reflection coefficient, cross-polarization reflection coefficient, as well as PCR, were shown in Fig. 6. It can be clearly seen from Fig. 6 that the measurement results are consistent with the simulation data.

To better explain the working mechanism of the CPC, the surface current density distribution at the SRR plane and the backplane at three peak frequencies (8.2 GHz//11.8 GHz//16.4 GHz) were simulated, as shown in Fig. 7. Figures in the top row of Fig. 7 show the current density distribution on the surface of the unit resonance structure, and figures in the second row show the current density distribution on the surface of the backplane. By comparing the current density direction on the SRR structure to that on the backplane, the resonance type can be determined

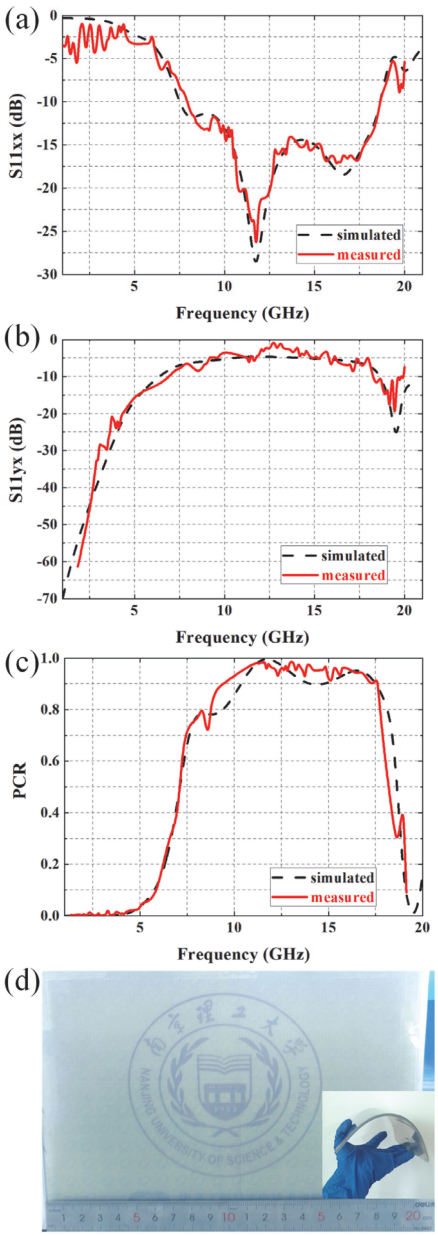

Fig. 6. (a) The photo shows optical transparency and mechanical flexibility of the fabricated sample. Comparison of the experimental and simulated spectra of (b) co-polarization S11; (c) cross-polarization S11; (d) PCR.

[24]–[27]. It can be seen from Fig. 7 that at 8.2 GHz and 16.4 GHz, the largest surface current density appears on the arm in the *y*-direction of the middle SRR structure, which is opposite to the backplane current density direction, effectively forming a magnetic dipole. This means that magnetic resonance is generated at 8.2 GHz and 16.4 GHz. While at 11.8 GHz, the largest surface current density appears on the arm in the *x*-direction of the middle SRR structure, which is the same as the backplane current density direction, effectively forming an electric dipole. This means that electrical resonance is generated at 11.8 GHz.

In addition, as can be seen in the figure, most of the current on the ring is along the *y* direction, which also indicates that

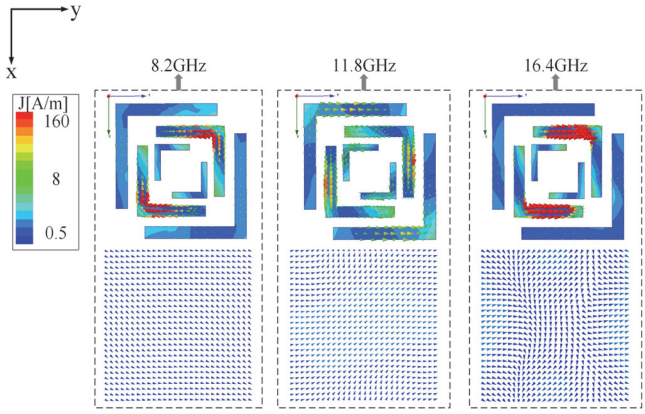

Fig. 7. The surface current density distribution of the SRR and the backplane at three peak frequencies (8.2 GHz//11.8 GHz//16.4 GHz).

the *x*-direction polarization incident electromagnetic wave has been successfully conversed into *y*- direction polarization after passing through the structure [28]–[29]. Through optimization of the geometric parameters of the resonance structure on the surface, the phase difference between the *x* and *y* components of the reflected EM waves can be adjusted to 180°, resulting in the generation of polarization transformation [14]–[15].

IV. Conclusion

In this work, a multilayer SRR-structure CPC was simulated, designed by ANSYS HFSS and fabricated by laser etching, showing a polarization conversion ratio greater than 77% in the range of (7.8-18.2) GHz. The experimental results are consistent with the software simulation data. In addition, the designed CPC is insensitive to oblique incidence within 45°, and has the advantages of broadband, optically transparent and mechanically flexible.

References

[1] R. T. Ako *et al.*, "Broadband and wide-angle reflective linear polarization converter for terahertz waves," *APL Photon.*, vol. 4, no. 9, 2019, Art. no. 096104.
[2] H. Wang and Y. Cheng, "Single-layer dual-band linear-to-circular polarization converter with wide axial ratio bandwidth and different polarization modes," *IEEE Trans. Antennas Propag.*, vol. 67, no. 6, pp. 4296–4301, 2019.
[3] X. Huang, D. Z. H.Yang, and Y. Luo, "Ultrathin dual-band metasurface polarization converter," *IEEE Trans. Antennas Propag.*, vol. 67, no. 7, pp. 4636–4641, Jul. 2019.
[4] Y. Jia *et al.*, "Ultra-wideband and high-efficiency polarization rotator based on metasurface," *Appl. Phys. Lett.*, vol. 109, no. 5, 2016, Art. no. 051901.
[5] Y. Ren, "Application of metamaterials in designing antenna and controling electromagnetic wave," in *Proc. Northwestern Polytechnical Univ.*, 2017, pp. 23–24.
[6] X. Ding *et al.*, "Ultrathin Pancharatnam–Berry metasurface with maximal cross-polarization efficiency," *Adv. Mater.*, vol. 27, no. 7, pp. 1195–1200, 2015.
[7] M. Mutlu and E. Ozbay, "A transparent 90 polarization rotator by combining chirality and electromagnetic wave tunneling," *Appl. Phys. Lett.*, vol. 100, no. 5, pp. 051909-1–051909-4, 2012.
[8] Z. Wei, Y. Cao, Y. Fan, X. Yu, and H. Li, "Broadband polarization transformation via enhanced asymmetric transmission through arrays of twisted complementary split-ring resonators," *Appl. Phys. Lett.*, vol. 99, no. 22, 2011, Art. no. 221907.
[9] R. H. Fan *et al.*, "Freely tunable broadband polarization rotator for terahertz waves," *Adv. Mater.*, vol. 27, no. 7, pp. 1201–1206, 2015.

[10] C. Huang *et al.*, "Break through the limitation of Malus' law with plasmonic polarizers," *Adv. Opt. Mater.*, vol. 2, no. 8, pp. 723–728, 2014.
[11] S. Abadi and N. Behdad, "Wideband linear-to-circular polarization converters based on miniaturized-element frequency selective surfaces," *IEEE Trans. Antennas Propag.*, vol. 64, no. 2, pp. 525–534, Feb. 2016.
[12] S. Teng *et al.*, "Conversion between polarization states based on a metasurface," *Photon. Res.*, vol. 7, no .3, pp. 246–250, 2019.
[13] H. X. Xu *et al.*, "Interference-assisted kaleidoscopic meta-plexer for arbitrary spin-wavefront manipulation" *Light: Sci. Appl.*, vol. 8, no. 1, pp. 1–10, 2019.
[14] M. Liu *et al.*, "Temperature-controlled asymmetric transmission of electromagnetic waves" *Sci. Reports*, vol. 9, no. 1, pp. 1–9, 2019.
[15] M. Chen *et al.*, "Wideband tunable cross polarization converter based on a graphene metasurface with a hollow-carved 'H' array" *IEEE Photon. J.*, vol. 9, no. 5, Oct. 2017, Art no. 4601011.
[16] C. Yang *et al.*, "Wideband tunable mid-infrared cross polarization converter using rectangle-shape perforated graphene" *Opt. Exp.*, vol. 24, no. 15, pp. 16913–16922, 2016.
[17] S. Bhattacharyya, S. Ghosh, and K. V. Srivastava, "A wideband cross polarization conversion using metasurface" *Radio Sci.*, vol. 52, no. 11, pp. 1395–1404, 2017.
[18] J. Hao *et al.*, "Manipulating electromagnetic wave polarizations by anisotropic metamaterials" *Phys. Rev. Lett.*, vol. 99, no. 6, 2007, Art. no. 063908.
[19] M. W. Chen, Y. F. Chau, and D. P. Tsai "Three-dimensional analysis of scattering field interactions and surface plasmon resonance in coupled silver nanospheres," *Plasmonics*, vol. 3, no. 4, pp. 157–164, 2008.
[20] C. Yuan-Fong *et al.*, "Tailoring surface plasmon resonance and dipole cavity plasmon modes of scattering cross section spectra on the single solid-gold/gold-shell nanorod," *J. Appl. Phys.*, vol. 120, no. 9, pp. 1–9, 2016.
[21] M. R. Soheilifar and R. A. Sadeghzadeh, "Design, fabrication and characterization of stacked layers planar broadband metamaterial absorber at microwave frequency," *AEU - Int. J. Electron. Commun.*, vol. 69, no. 1, pp. 126–132, 2015.
[22] X. Gao, W. L. Yang, H. F. Ma, Q. Cheng, X. H. Yu, and T. J. Cui, "A reconfigurable broadband polarization converter based on an active metasurface," *IEEE Trans. Antennas Propag.*, vol. 66, no. 11, pp. 6086–6095, Nov. 2018.
[23] Q. Zheng, C. Guo, and J. Ding, "Wideband metasurface-based reflective polarization converter for linear-to-linear and linear-to-circular polarization conversion," *IEEE Antennas Wireless Propag. Lett.*, vol. 17, no. 8, pp. 1459–1463, Aug. 2018.
[24] C. L. Holloway, E. F. Kuester, and A. Dienstfrey, "Characterizing metasurfaces/metafilms: The connection between surface susceptibilities and effective material properties," *IEEE Antennas Wireless Propag. Lett.*, vol. 10, pp. 1507–1511, 2011.
[25] S. Bhattacharyya, S. Ghosh, and K. V. Srivastava, "An ultra-thin polarization independent metamaterial absorber for triple band applications," in *Proc. IEEE Appl. Electromagnetics Conf.,* 2013, pp. 1–2.
[26] Y. Z. Ho *et al.*, "Tunable plasmonic resonance arising from broken-symmetric silver nanobeads with dielectric cores," *J. Opt.*, vol. 14, no. 11, pp. 114010-1–114010-6, 2012.
[27] M. J. Sung *et al.*, "Surface plasmon resonance in a hexagonal nanostructure formed by seven core shell nanocylinders," *Appl. Opt.*, vol. 49,no. 5, pp. 920–926, 2010.
[28] P. Xu, S. Y. Wang, and G. Wen, "A linear polarization converter with near unity efficiency in microwave regime," *J. Appl. Phys.*, vol. 121, no. 14, pp. 1804–1949, 2017.
[29] T. Noishiki, R. Kuse, and T. Fukusako, "Wideband metasurface polarization converter with double-square-shaped patch elements," *Prog. electromagnetics Res. C*, vol. 105, pp. 47–58, 2020.